Supplementary Information

Engineering and optimising barium cerate-supported cobalt catalyst for ammonia synthesis

Hubert Ronduda [a]*, Małgorzata Lemańska [a], Urszula Ulkowska [a], Wojciech Patkowski [a], Weronika Bulejak [a], Andrzej Ostrowski [a], Jacek Sikorski [a], Kamil Sobczak [b], Milena Ojrzyńska [c], Dariusz Moszyński [d], Wioletta Raróg-Pilecka [a]

[a] *Warsaw University of Technology, Faculty of Chemistry, Noakowskiego 3, 00-664 Warsaw, Poland*

[b] *University of Warsaw Biological and Chemical Research Centre, Żwirki i Wigury 101, 02-089 Warsaw, Poland*

[c] *Institute of Optoelectronics, Military University of Technology, Kaliskiego 2, 00-908 Warsaw, Poland*

[d] *West Pomeranian University of Technology in Szczecin, Faculty of Chemical Technology and Engineering, Department of Inorganic Chemical Technology and Environment Engineering, Piastów Ave. 42, 71-065 Szczecin, Poland*

*Corresponding author

e-mail: hubert.ronduda@pw.edu.pl

tel. +48 22 234 7602

Number of pages: **11**

Number of figures: **13**

Number of tables: **10**

Table S1. Cobalt loadings in the catalysts determined by ICP-MS.

Catalyst	Nominal Co content (wt%)	Experimental Co content (wt%)
10Co-WI	10	8.55 ± 0.51
10Co-PM	10	10.47 ± 0.19
10Co-DP	10	10.29 ± 0.78
20Co-DP	20	19.53 ± 0.57
30Co-DP	30	28.21 ± 0.49
40Co-DP	40	40.08 ± 0.89
50Co-DP	50	49.36 ± 2.58

Table S2. Quantitative H_2-TPD results of 10Co-DP, 10Co-WI, and 10Co-PM catalysts.

Catalyst	H_2 chemisorption (μmol g_{cat}^{-1})			LT/HT ratio [d]
	LT [a]	HT [b]	LT + HT [c]	
10Co-DP	17.1	32.5	49.6	0.53
10Co-WI	26.4	46.1	72.5	0.57
10Co-PM	8.9	28.5	37.4	0.31

[a] H_2 desorption at low temperatures. [b] H_2 desorption at high temperatures. [c] Total H_2 desorption. [d] Ratio of the H_2 desorption at low temperature to the H_2 desorption at high temperature.

Table S3. Quantitative H_2-TPD results of the *x*Co-DP and 30Co-WI catalysts reduced at 600 °C.

Catalyst	H_2 chemisorption (μmol g_{cat}^{-1})			LT/HT ratio [d]
	LT [a]	HT [b]	LT + HT [c]	
10Co-DP	17.1	32.5	49.6	0.53
20Co-DP	26.2	45.0	71.2	0.58
30Co-DP	37.6	44.9	82.5	0.84
30Co-WI	24.9	40.5	65.4	0.62
40Co-DP	41.3	43.0	84.3	0.96
50Co-DP	41.0	38.5	79.5	1.06

[a] H_2 desorption at low temperatures. [b] H_2 desorption at high temperatures. [c] Total H_2 desorption. [d] Ratio of the H_2 desorption at low temperature to the H_2 desorption at high temperature.

Table S4. Comparison of the catalytic performance of different supported catalysts for NH_3 synthesis.

Entry	Active metal	Catalyst	Metal content (wt%)	Temperature (°C)	Pressure (MPa)	GHSV (mL g_{cat}^{-1} h^{-1})	NH_3 synthesis rate ($mmol_{NH_3}$ g_{cat}^{-1} h^{-1})	Ref.
1	Fe	Fe/K(3)/MgO	20	350	1.0	72,000	17.5	[1]
2		Fe/MgO					2.7	
3	Ru	Ru/Pr_2O_3	5	390	0.9	18,000	15.2	[2]
4		Ru/CeO_2					7.4	
5		Ru/MgO					1.5	
6		$Ru/BaZrO_3$	4	400	3.0	—	15.3	[3]
7		Ru/MgO					8.4	
8		Ru/CeO_2					8.4	
9	Co	Co/K(1)/MgO	20	400	1.0	72,000	3.1	[4]
10		Co/K(3)/MgO					2.7	
11		Co/MgO					1.6	
12		$Co/Ba/La_2O_3$	20	350	1.0	72,000	19.3	[5]
13		Co/La_2O_3					2.8	
14		Co/La_2O_3	10	470	6.3	140,000	47.0	[6]
15		$CoNd_2O_3$					17.6	
16		Co/Sm_2O_3					8.2	
17		Co/Eu_2O_3					10.6	
18		Co/Gd_2O_3					10.6	
19		$Co/MgO–La_2O_3$	10	470	6.3	140,000	45.8	[7]
20			20				63.7	
21			30				83.6	
22			40				108.8	
23			50				105.4	
24		Co/Nd_2O_3	10	470	6.3	140,000	59.3	[8]
25			20				81.6	
26			30				74.6	
27			40				83.4	
28			50				106.9	
29		$Co/BaCe_{0.9}Sm_{0.1}O_{3-\delta}$	10	470	6.3	140,000	91.7	This work
30			20				182.0	
31			30				235.7	
32			40				281.7	
33			50				262.7	

** Dash (—) indicates no data.*

Table S5. Comparison of the performance of the cobalt catalyst with the industrial KM1R catalyst for NH_3 synthesis.

Catalyst	Metal content (wt%)	Pressure (MPa)	Temperature (°C)	GHSV (mL g_{cat}^{-1} h^{-1})	NH_3 synthesis rate		Ref.
					$mmol_{NH_3}$ g_{cat}^{-1} h^{-1}	$mmol_{NH_3}$ g_{metal}^{-1} h^{-1}	
Industrial Fe catalyst (KM1R) [a]	94	10	400	~80,000	158.0	168.1	[9]
$Co/BaCe_{0.9}Sm_{0.1}O_{3-\delta}$	40	6.3	400	140,000	115.8	288.9	This work

[a] KM1R is a triply promoted iron catalyst containing ~2.8% CaO, 0.60% K_2O, 2.5% Al_2O_3, and 94% Fe.

Table S6. Peak maximum temperatures and hydrogen consumptions from H_2-TPR analyses for *x*Co-DP.

Sample	Peak maximum temperature (°C)		Hydrogen consumption ($cm^3\ g^{-1}$)			Co loading (wt%) [a]
	Peak I	Peak II	Peak I	Peak II	Total	
10Co-DP	299	387	0.5	1.6	2.1	9.5
20Co-DP	307	383	1.0	3.2	4.2	20.1
30Co-DP	316	456	1.4	4.6	6.0	29.7
40Co-DP	318	459	1.9	6.3	8.2	42.7
50Co-DP	323	465	2.2	7.4	9.6	51.1

[a] Co loading in the catalysts.

Table S7. Mass losses and mass gains during the reduction and oxidation processes of *x*Co-DP.

Sample	Mass loss during the reduction step (%)	Mass gain during the oxidation step (%)	Co loading (wt%) [a]
10Co-DP	5.2	3.5	10.1
20Co-DP	9.0	6.7	20.1
30Co-DP	12.1	9.5	30.3
40Co-DP	15.3	12.4	41.3
50Co-DP	18.3	15.3	52.5

[a] Co loading in the catalysts. Calculated based on the mass gain during the oxidation step.

Table S8. Quantitative H_2-TPD results of the *x*Co-DP catalysts reduced at 550 °C.

Catalyst	H_2 chemisorption ($\mu mol\ g_{cat}^{-1}$)			LT/HT ratio [d]
	LT [a]	HT [b]	LT + HT [c]	
10Co-DP	18.3	31.5	49.8	0.58
20Co-DP	35.3	37.8	73.1	0.93
30Co-DP	50.7	33.2	83.9	1.53
40Co-DP	55.0	34.9	89.9	1.58
50Co-DP	51.4	35.7	87.1	1.44

[a] H_2 desorption at low temperatures. [b] H_2 desorption at high temperatures. [c] Total H_2 desorption. [d] Ratio of the H_2 desorption at low temperature to the H_2 desorption at high temperature.

Table S9. Effect of catalyst reduction temperature on the NH_3 synthesis performance over the *x*Co-DP catalysts.

Catalyst	Ammonia synthesis rate [a] ($g_{NH_3}\ g_{cat}^{-1}\ h^{-1}$)	
	Catalysts reduced at 550 °C	Catalysts reduced at 600 °C
10Co-DP	1.41	1.56
20Co-DP	2.83	3.10
30Co-DP	3.73	4.01
40Co-DP	4.44	4.80
50Co-DP	4.12	4.47

[a] Reaction conditions: pressure, 6.3 MPa; temperature, 470 °C; synthesis gas, H_2/N_2 = 3 with a flow rate of 70 L h^{-1}.

Table S10. Quantitative N_2-TPD results of the *x*Co-DP catalysts reduced at 600 °C.

Catalyst	N_2 chemisorption (μmol g_{cat}^{-1}) [a]
10Co-DP	5.8
20Co-DP	11.2
30Co-DP	12.9
40Co-DP	15.0
50Co-DP	14.4

[a] Total N_2 desorption.

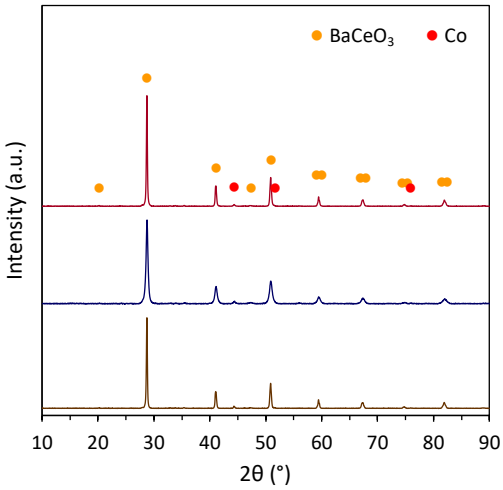

Figure S1. XRD patterns of the 10Co-DP, 10Co-WI and 10Co-PM catalysts. The orange dot (●) indicates $BaCeO_3$, and the red dot (●) indicates fcc-Co.

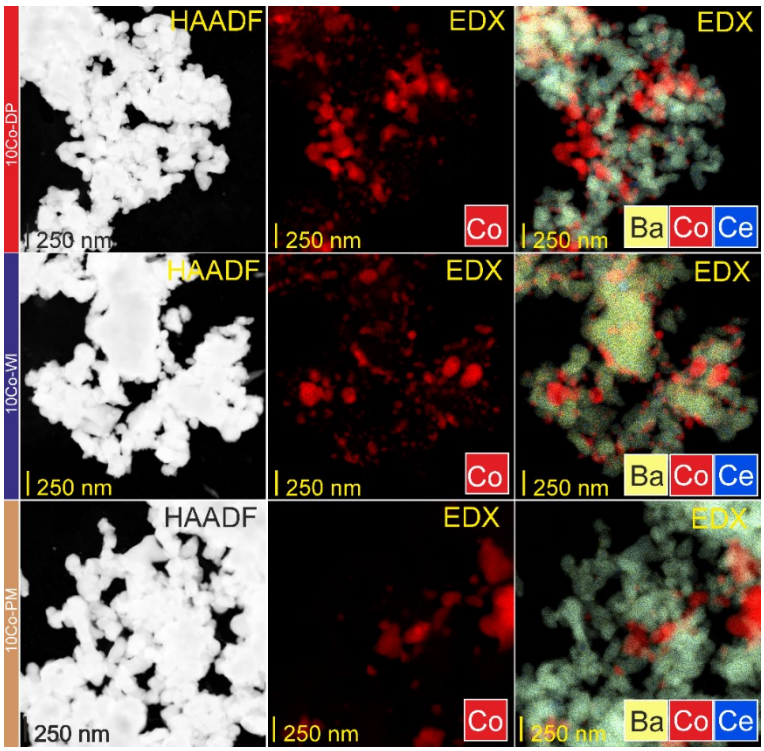

Figure S2. HAADF-STEM image and corresponding EDX maps of the 10Co-DP, 10Co-WI and 10Co-PM catalysts.

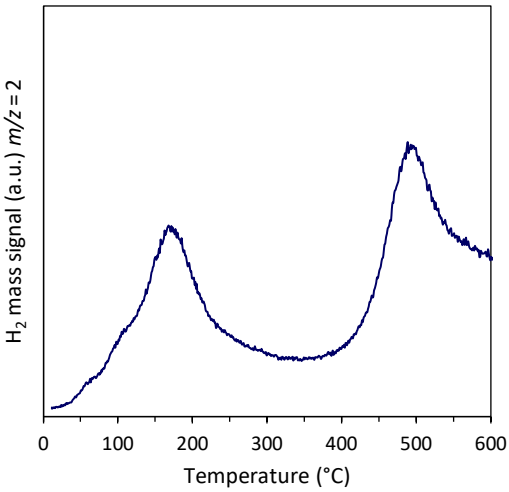

Figure S3. H_2-TPD analysis of the 30Co-WI catalyst reduced at 600 °C.

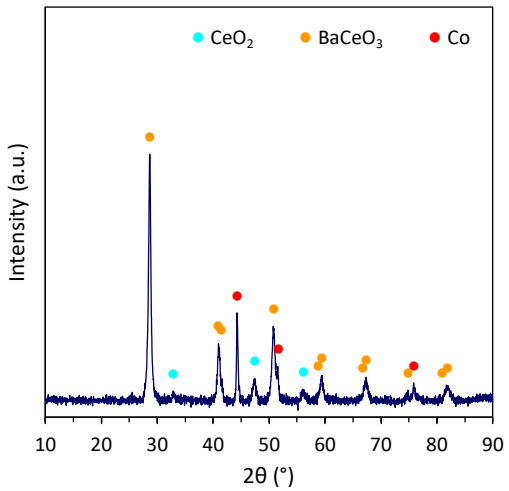

Figure S4. XRD pattern of the 30Co-WI catalyst. The turquoise dot (●) indicates CeO_2, the orange dot (●) indicates $BaCeO_3$, and the red dot (●) indicates fcc-Co.

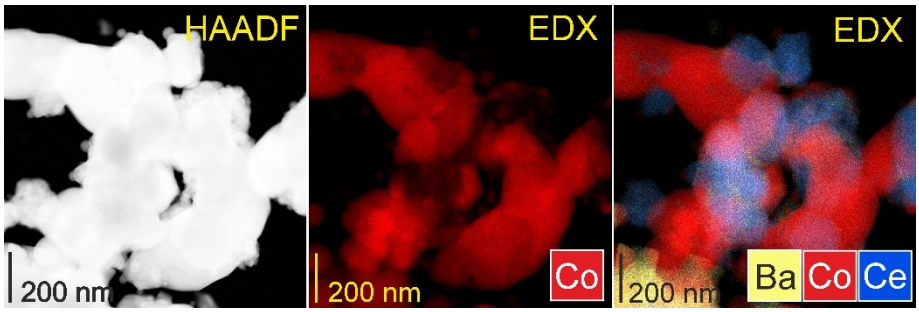

Figure S5. HAADF-STEM image and corresponding EDX maps of the 30Co-WI catalyst.

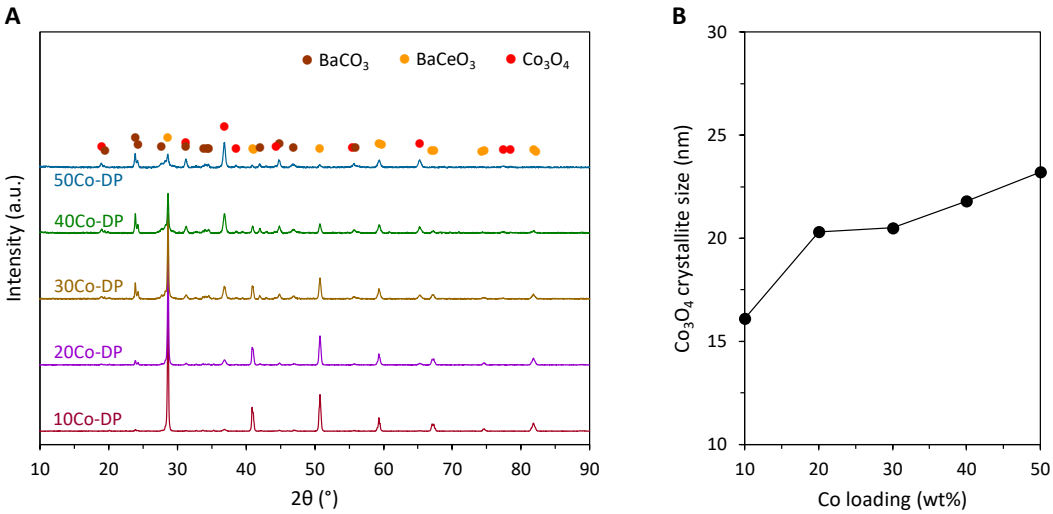

Figure S6. (A) XRD patterns of the *x*Co-DP pre-catalysts. The brown dot (●) indicates $BaCO_3$, the orange dot (●) indicates $BaCeO_3$, and the red dot (●) indicates Co_3O_4. (B) The dependence of Co loadings on the size of Co_3O_4 crystallites. The Co_3O_4 crystallite size was determined from the (311) reflection. For all the pre-catalysts, the diffraction peaks attributable to $BaCeO_3$ in the *Pmcn* space group were clearly visible. There were also peaks related to the Co_3O_4 phase (PDF 74-1656), and minor diffraction peaks assignable to $BaCO_3$. The Co_3O_4 crystallite size increased with increasing Co loading, from 16 nm for 10 wt% Co to 23 nm for 50 wt% Co.

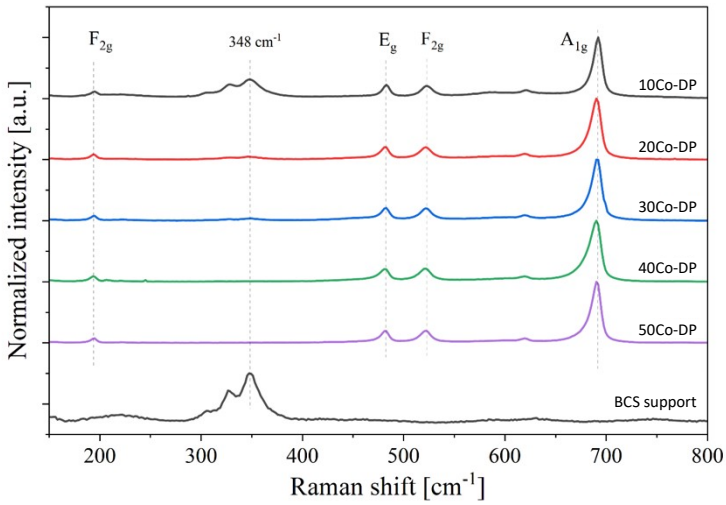

Figure S7. Raman spectra of the BCS support and *x*Co-DP pre-catalyst. Averaged Raman spectra were collected from 400 points on the surface for the pre-catalysts with varying Co loadings, with the characteristic F_{2g}, E_g, and A_{1g} vibrational modes marked. All the pre-catalysts exhibited the characteristic Raman modes of Co_3O_4 [10,11]: the F_{2g} mode at ~190 cm^{-1}, the E_g and F_{2g} modes in the 450–520 cm^{-1} region, and the dominant A_{1g} mode located around ~690–700 cm^{-1}. In comparison with the literature data [10], the bands are shifted by approximately 10–20 cm^{-1} towards higher wavelengths. The peak at 690–700 cm^{-1} corresponds to CoO_6 vibrations of the octahedral sites (A_{1g}), whereas the peak at 190 cm^{-1} is associated with CoO_4 vibrations of the tetrahedral sites (F_{2g}). No significant changes are observed in the Raman modes; their positions and shapes remain essentially unchanged across Co loadings. On the contrary, distinct differences were evident in the Raman modes related to the BCS support. As the Co loading increased, the support features, two modes at 327 cm^{-1} and 348.2 cm^{-1}, gradually diminished and eventually disappeared. In the averaged spectra, the substrate modes remained visible for the 10Co-DP, 20Co-DP, and 30Co-DP pre-catalysts, but disappeared as the Co loading increased further, indicating a more complete surface coverage by cobalt oxide.

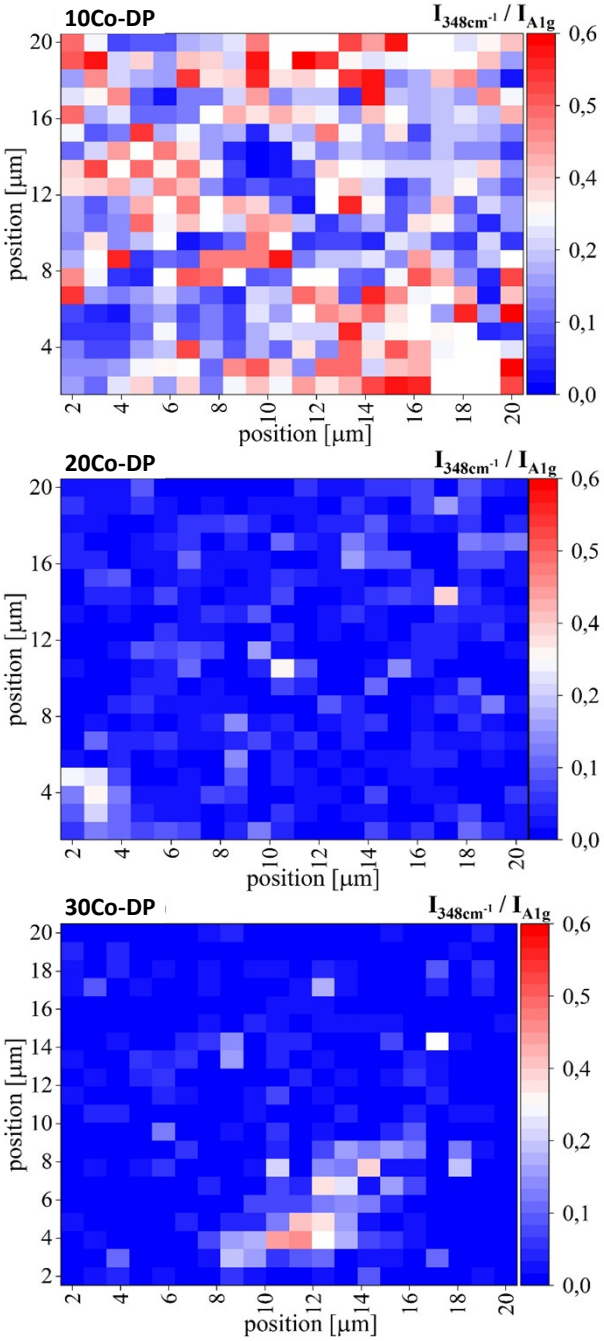

Figure S8. Raman intensity maps showing the spatial distribution of the $I_{348cm^{-1}}/I_{A_{1g}}$ ratio for the *x*Co-DP (*x* = 10, 20, and 30) pre-catalysts. Higher values of the ratio indicate a stronger contribution of the 348 cm^{-1} mode of BCS support relative to the A_{1g} mode of Co_3O_4. Each map reflects the relative contribution of the 348 cm^{-1} mode related to support compared to the A_{1g} mode of Co_3O_4 at each measurement point, with spectra collected every 1 µm across the surface. The 10Co-DP map exhibited strong spatial variability, with numerous red and white regions indicating a high relative intensity of the 348 cm^{-1} mode of BCS support. This suggests that at low cobalt loading, the support signal remains clearly detectable. For 20Co-DP, the map becomes significantly more homogeneous and predominantly blue, showing that the contribution of the support-related mode is much weaker across most of the surface. Only a few isolated spots displayed locally elevated support-related intensity. This behaviour indicates a more continuous cobalt(II,III) oxide distribution compared to 10Co-DP. The 30Co-DP map shows an even stronger suppression of the support signal, with the majority of the area appearing deep blue. Only small, localised regions exhibit a noticeable signal contribution of support. This aligns

with the averaged Raman spectra, in which the support modes remained faintly visible up to a 30 wt% Co loading but were already significantly reduced (**Figure S7**).

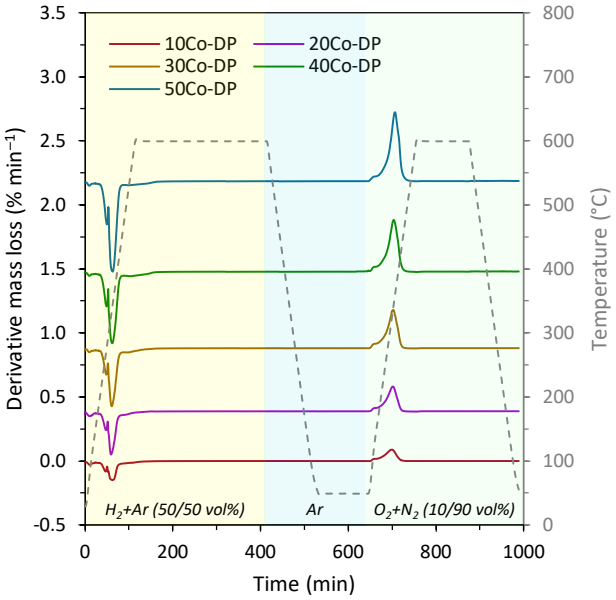

Figure S9. DTG analyses of the *x*Co-DP pre-catalysts.

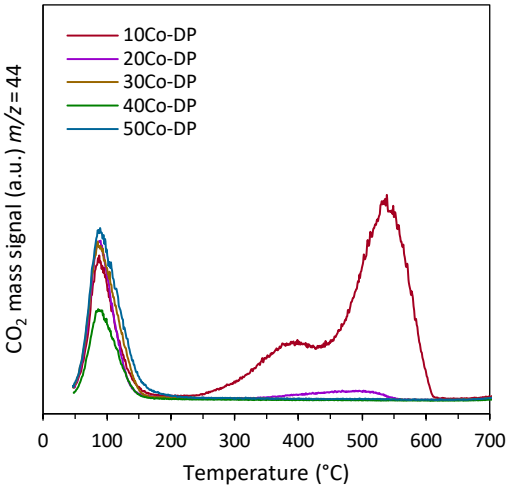

Figure S10. CO_2-TPD profiles of *x*Co-DP catalysts.

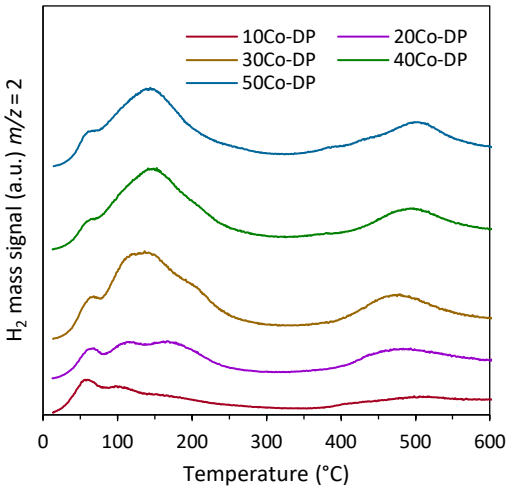

Figure S11. H_2-TPD analyses of the *x*Co–DP catalysts reduced at 550 °C.

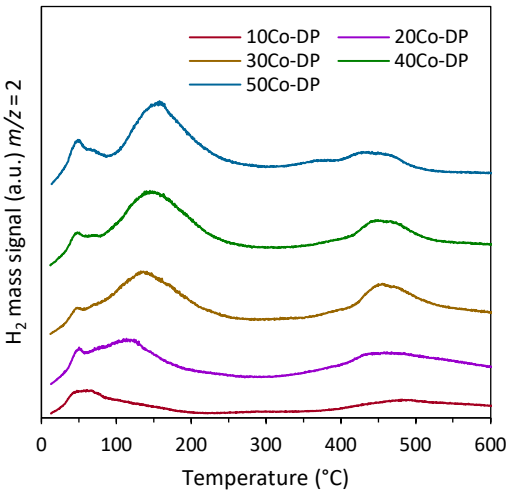

Figure S12. H_2-TPD analyses of the *x*Co–DP spent catalysts (after ammonia synthesis reaction).

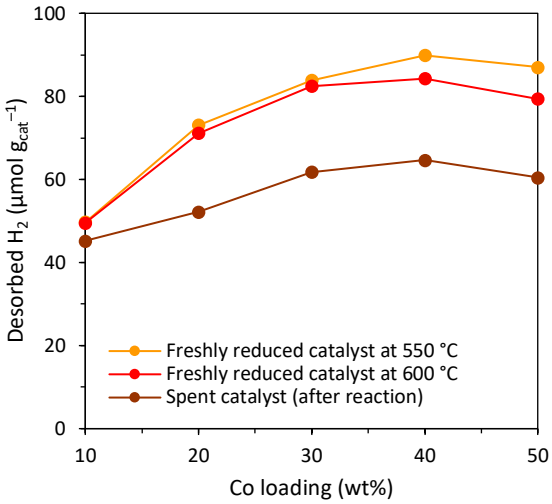

Figure S13. Dependence of H_2 desorption from H_2-TPD analyses on Co loading for the freshly reduced and spent *x*Co-DP catalysts.

References

[1] K. Era et al., Catalytic Behavior of K-doped Fe/MgO Catalysts for Ammonia Synthesis Under Mild Reaction Conditions, *ChemSusChem*, 2023, **16**, e202300942. https://doi.org/10.1002/cssc.202300942

[2] K. Sato et al., A low-crystalline ruthenium nano-layer supported on praseodymium oxide as an active catalyst for ammonia synthesis, *Chem. Sci.*, 2017, **8**, 674-679. https://doi.org/10.1039/C6SC02382G

[3] Z. Wang et al., Highly effective perovskite-type $BaZrO_3$ supported Ru catalyst for ammonia synthesis, *Appl. Catal. A Gen.*, 2013, **458**, 130–136. https://doi.org/10.1016/j.apcata.2013.03.037

[4] T. Shibata et al., Effect of Potassium Doping on the Surface Structure and Ammonia Synthesis Activity of Co/MgO, *ACS Omega*, 2025, **10**, 53113–53121. https://doi.org/10.1021/acsomega.5c07671

[5] S.-i. Miyahara et al., Co Nanoparticle Catalysts Encapsulated by BaO–La_2O_3 Nanofractions for Efficient Ammonia Synthesis Under Mild Reaction Conditions, *ACS Omega*, 2022, **7**, 24452–24460. https://doi.org/10.1021/acsomega.2c01973

[6] W. Patkowski et al., Toward Green ammonia synthesis – exploring the influence of lanthanide oxides as supports on the cobalt catalysts properties, *J. CO_2 Util*., 2024, **80**, 102699. https://doi.org/10.1016/j.jcou.2024.102699

[7] H. Ronduda et al., On the effect of metal loading on the performance of Co catalysts supported on mixed MgO–La_2O_3 oxides for ammonia synthesis, *RSC Adv.*, 2022, **12**, 33876–33888. https://doi.org/10.1039/D2RA06053A

[8] W. Patkowski et al., The Influence of Active Phase Content on Properties and Activity of Nd_2O_3-Supported Cobalt Catalysts for Ammonia Synthesis, *Catalysts* 2023, **13**, 405. https://doi.org/10.3390/catal13020405

[9] J. Sehested et al., Ammonia Synthesis over a Multipromoted Iron Catalyst: Extended Set of Activity Measurements, Microkinetic Model, and Hydrogen Inhibition, *J. Catal.*, 1999, **188**, 83–89. https://doi.org/10.1006/jcat.1999.2628

[10] M. Wu et al., Investigation of synergistic effects and high performance of La-Co composite oxides for toluene catalytic oxidation at low temperature. *Environ. Sci. Pollut. Res.*, 2019, **26**, 12123–12135. https://doi.org/10.1007/s11356-019-04672-7

[11] Y. Zheng et al., Complete combustion of methane over Co_3O_4 catalysts: Influence of pH values, *J. Alloys Compd*., 2018, **734**, 112–120. https://doi.org/10.1016/j.jallcom.2017.11.008